

Quantitative spectroscopy of Deneb [★]

F. Schiller and N. Przybilla

Dr. Remeis-Sternwarte Bamberg, Sternwartstr. 7, D-96049 Bamberg, Germany

Received ... ; accepted ...

ABSTRACT

Context. Quantitative spectroscopy of luminous BA-type supergiants offers a high potential for modern astrophysics. Detailed studies allow the evolution of massive stars and galactochemical evolution and permits the cosmic distance scale to be constrained observationally.

Aims. A detailed and comprehensive understanding of the atmospheres of BA-type supergiants is required in order to use this potential properly. The degree to which we can rely on quantitative studies of this class of stars as a whole depends on the quality of the analyses for benchmark objects. We constrain the basic atmospheric parameters and fundamental stellar parameters, as well as chemical abundances of the prototype A-type supergiant Deneb to unprecedented accuracy by applying a sophisticated analysis methodology, which has recently been developed and tested.

Methods. The analysis is based on high-S/N and high-resolution spectra in the visual and near-IR. Stellar parameters and abundances for numerous astrophysically interesting elements are derived from synthesis of the photospheric spectrum using a hybrid non-LTE technique, i.e. line-blanketed LTE model atmospheres and non-LTE line formation. Multiple metal ionisation equilibria and numerous hydrogen lines from the Balmer, Paschen, Brackett, and Pfund series are made to match simultaneously for the stellar parameter determination. The stellar wind properties are derived from H α line-profile fitting using line-blanketed hydrodynamic non-LTE models. Further constraints come from matching the photospheric spectral energy distribution from the UV to the near-IR *L* band.

Results. The atmospheric parameters of Deneb are tightly constrained: effective temperature $T_{\text{eff}} = 8525 \pm 75$ K, surface gravity $\log g = 1.10 \pm 0.05$, microturbulence $\xi = 8 \pm 1$ km s⁻¹, macroturbulence, and projected rotational velocity $v \sin i$ are both 20 ± 2 km s⁻¹. The abundance analysis gives helium enrichment by 0.10 dex relative to solar and an N/C ratio of 4.44 ± 0.84 (mass fraction), implying strong mixing with CN-processed matter. The heavier elements are consistently underabundant by ~ 0.20 dex compared to solar. Peculiar abundance patterns, which were derived in previous analyses to exist in Deneb, cannot be confirmed. Accounting for non-LTE effects is essential for removing systematic trends in the abundance determination, for minimising statistical 1σ -uncertainties to ≤ 10 -20% and for establishing all ionisation equilibria at the same time.

Conclusions. A luminosity of $(1.96 \pm 0.32) \times 10^5 L_{\odot}$, a radius of $203 \pm 17 R_{\odot}$, and a current mass of $19 \pm 4 M_{\odot}$ are derived. Comparison with stellar evolution predictions suggests that Deneb started as a fast-rotating late O-type star with $M^{\text{ZAMS}} \approx 23 M_{\odot}$ on the main sequence and is currently evolving to the red supergiant stage.

Key words. Stars: supergiants, early-type, fundamental parameters, abundances, evolution, individual (Deneb)

1. Introduction

Massive stars are fundamental for the energy and momentum balance of galaxies. They represent important sources of ionising radiation and mass outflow through stellar winds. The final supernova explosions contribute to the dynamics of the interstellar medium (ISM), stimulate star formation, and enrich the ISM with heavy elements. Massive stars are therefore major drivers of the cosmic cycle of matter. Moreover, because of their high luminosities they can be observed over long distances, consequently providing powerful indicators for the studying stellar and galactochemical evolution in a wide variety of galactic environments.

Supergiants of spectral types B and A (BA-type supergiants) are among the visually brightest massive stars. Therefore, they are particularly interesting for extragalactic astronomy. Spectroscopy of individual BA-type supergiants is feasible in

galaxies well beyond the Local Group using large ground-based telescopes (Bresolin et al. 2001, 2002). So far, stellar abundances were compared to those from H II regions, and abundance gradients were measured (Urbaneja et al. 2005). Moreover, BA-type supergiants show a high potential as standard candles for distance determinations, via application of the flux-weighted gravity-luminosity relationship (FGLR, Kudritzki et al. 2003) or via the wind momentum-luminosity relationship (WLR, Kudritzki et al. 1999). A crucial advantage over classical indicators such as Cepheids is the possibility for a direct determination of metallicity and interstellar reddening from the quantitative analysis, allowing the systematic error budget to be reduced.

A comprehensive understanding of the atmospheres of BA-type supergiants has to be developed as the basis for detailed quantitative analyses in order to use their high potential as versatile indicators of stellar and galactic evolution and as distance indicators. The degree to which we can rely on quantitative analyses of BA-type supergiants in general depends on the quality and self-consistency of analysing benchmark objects, stars with comprehensive observational data of the highest quality. In this respect, the brightest A-type supergiant Deneb (A2 Ia) represents

Send offprint requests to: F. Schiller, schiller@sternwarte.uni-erlangen.de

[★] Based on observations collected at the Centro Astronómico Hispano Alemán (CAHA) at Calar Alto, operated jointly by the Max-Planck Institut für Astronomie and the Instituto de Astrofísica de Andalucía (CSIC).

one of the crucial test cases for model atmosphere analyses of this class of stars.

Deneb is the best-studied A-type supergiant. Nevertheless, quantitative analyses using model atmospheres, from the pioneering work of Groth (1961) to the most recent study of Aufdenberg et al. (2002), find no consensus on atmospheric parameters and elemental abundances. Published values for the effective temperature range e.g. from 7635 K (Blackwell et al. 1980) to 10 080 K (Burnashev 1980), for the surface gravity from $\log g = 1$ (Zverko 1971) to 1.54 (Burnashev 1980).

Our aim is to apply recently introduced analysis methodology for BA-type supergiants (Przybilla 2002; Przybilla et al. 2006) on visual and near-IR spectra of the benchmark star Deneb. Stellar parameters and elemental abundances may thus be derived with unprecedented accuracy. In comparison with recent models of the evolution of massive stars accounting for mass loss and rotation (e.g. Heger & Langer 2000; Meynet & Maeder 2003) and the presence of magnetic fields (Heger et al. 2005; Maeder & Meynet 2005), this will allow the evolutionary status of Deneb to be discussed. In addition, the stellar wind properties of Deneb will be investigated quantitatively.

The paper is organised as follows. We describe the observational data in Sect. 2 and the derivation of the stellar parameters in Sect. 3, while the elemental abundance determination is presented in Sect. 4. Additional constraints from near-IR spectroscopy are considered in Sect. 5. We discuss the evolutionary status of Deneb in Sect. 6. Finally, the main results are summarised in Sect. 7.

2. Observations and data reduction

Our primary observational data for the quantitative analysis are high-resolution, high-S/N spectra taken on 21 September 2005 with the Fibre Optics Cassegrain Echelle Spectrograph (FOCES, Pfeiffer et al. 1998) on the 2.2 m-telescope at Calar Alto/Spain. Eight spectra were obtained at 1'' seeing conditions covering a wavelength range from 3860 to 9580 Å at resolving power $R = \lambda/\Delta\lambda \approx 40\,000$. After the reduction of each spectrum using routines from the FOCES-package (correction for bad pixels and cosmetics, subtraction of bias and dark current, flatfielding, wavelength calibration, rectification, and merging of all Echelle orders), the eight spectra were coadded, resulting in a final S/N ratio of about 600 throughout most of the spectral range. Cross-correlation of this spectrum to an appropriate synthetic spectrum at rest wavelength provides a correction for the radial velocity shift ($v_{\text{rad}} = 2.50 \text{ km s}^{-1}$). Comparison of our Echelle data (in particular around the Balmer lines) with a longslit spectrum¹ (at 1.8 Å resolution in the range from 3900 to 4600 Å taken at the Dark Sky Observatory, Appalachian State University) allows our continuum rectification to be verified, giving excellent agreement. Also, a good agreement with the spectroscopic atlas of Albayrak et al. 2003 is found.

Besides the spectra of September 2005, we can consider data taken with the same instrument on 26 September 2001. The comparison between these two spectra (Fig. 1) shows a variable P-Cygni profile of $H\alpha$, while the higher Balmer lines and the metal features remain almost unchanged. This implies that wind variability will not affect the analysis of the photospheric features in the present case. Our two spectra are representative of the states near maximum/minimum wind emission reported by Kaufer et al. (1996) from a 2-year long spectroscopic campaign on Deneb.

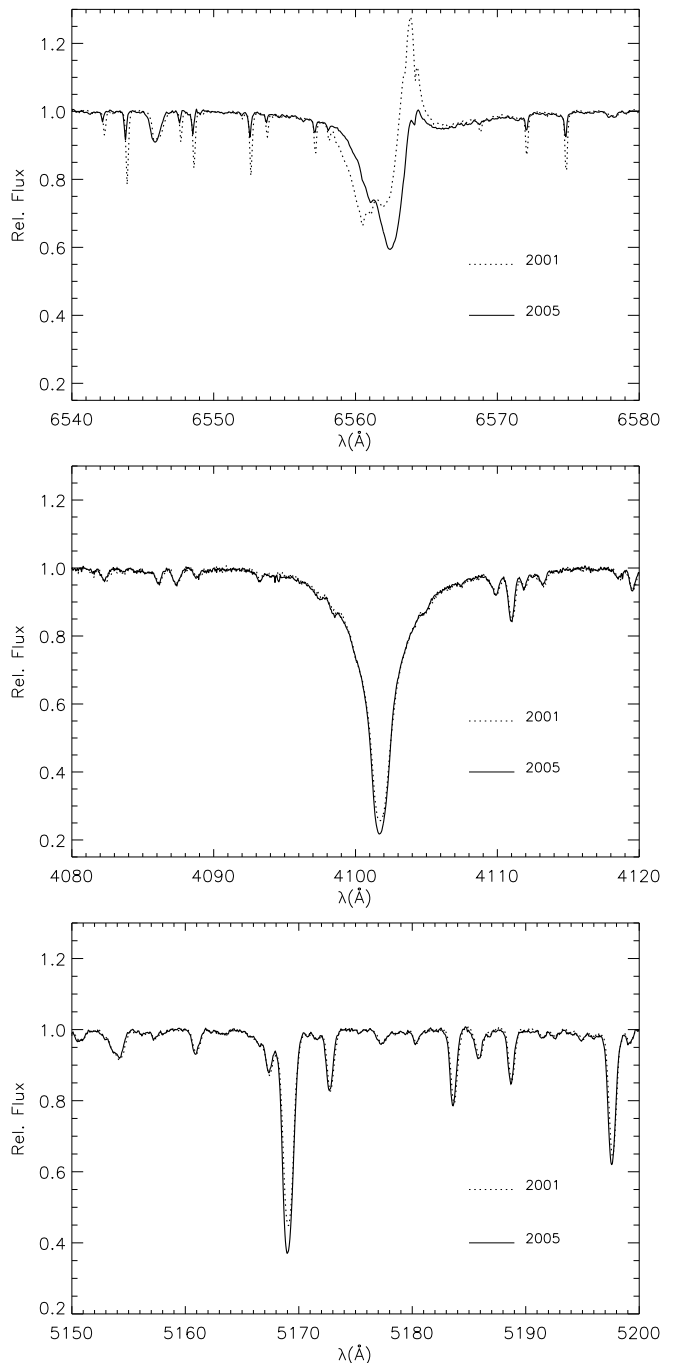


Fig. 1. Comparison between spectra of Deneb from 2001 (dotted) and 2005 (solid). Spectral regions around $H\alpha$ (upper), $H\delta$ (middle), and the $Mg\text{I}$ triplet (lower panel) are displayed. Note the numerous sharp telluric H_2O features in the $H\alpha$ region. The wind-dominated $H\alpha$ line shows a pronounced P-Cygni profile in 2001 and reduced emission in 2005. Only the cores of the higher Balmer lines and few of the strongest metal lines (like $\text{Fe II } \lambda 5169$) are affected by the variable stellar wind.

Photometric data, as well as UV and near-infrared spectra, are used to verify our analysis via spectral energy distribution fits and comparison with additional diagnostic spectral features. Here, the data considered are

1. flux-calibrated, low-dispersion spectra from 1150 to 1980 Å and from 1850 to 3290 Å, obtained by the IUE satellite

¹ available via http://stellar.phys.appstate.edu/Standards/std1_8.html

Table 1. Non-LTE model atoms.

Ion	Source
H	Przybilla & Butler (2004)
He I	Przybilla (2005)
C I/II	Przybilla et al. (2001b), Nieva & Przybilla (2006, 2007)
N I/II	Przybilla & Butler (2001)
O I	Przybilla et al. (2000)
Mg I/II	Przybilla et al. (2001a)
S II	Vrancken et al. (1996), with updated atomic data
Ti II	Becker (1998)
Fe II	Becker (1998)

(SWP09133 and LWR07864, respectively, as extracted from the INES archive²),

2. *UBV* photometry from Johnson et al. (1966) and *RIL* from Morel & Magnenat (1978), Strömgren photometry ($m_1, b-y, c_1$) from Hauck & Mermilliod (1998), and *JHK*-data from the Two Micron All Sky Survey (2MASS, Skrutskie et al. 2006),
3. high-quality spectra ($R \approx 3000 - 10\,000$, $S/N \sim 100$) in the *Jw*-, *H*-, and *K*-band (Fullerton & Najarro 1998) and a *K*-band spectrum ($R \approx 3000$) from Wallace & Hinkle (1997).

3. Stellar parameters

3.1. Basic atmospheric parameters

The basic atmospheric parameters, such as effective temperature T_{eff} , surface gravity $\log g$, microturbulent velocity ξ , helium abundance $n(\text{He})$, together with macroturbulent velocity ζ and projected rotational velocity $v \sin i$, are derived from a comparison of observation with model spectra. The synthetic spectra are computed using both LTE and non-LTE techniques.

The LTE model atmospheres are calculated with the ATLAS9 code (Kurucz 1993), in the version of M. Lemke as obtained from the CCP7 software library. Further modifications (Przybilla et al. 2001b) allow model convergence close to the Eddington limit to be obtained, which turns out to be crucial in the case of Deneb. The LTE model atmospheres are the basis for non-LTE line-formation computations with DETAIL and SURFACE (Giddings 1981; Butler & Giddings 1985; recently updated by K. Butler). Non-LTE model atoms according to Table 1 are considered. This hybrid non-LTE technique is able to reproduce observation at high quality with modest requirements for computing time, see Przybilla et al. (2006) for a detailed discussion. Line-formation calculations assuming LTE are also performed with SURFACE.

Several spectral features can be utilised for determining the basic atmospheric parameters via fits of synthetic spectra to observation. Ionisation equilibria of metals like Mg I/II, C I/II, N I/II (and other species showing spectral lines from two or more ionisation stages) are highly sensitive indicators for T_{eff} , as well as for $\log g$ in early A-type supergiants. The hydrogen lines are mainly sensitive to variations in $\log g$. The helium abundance has to be determined simultaneously with the other atmospheric parameters in order to minimise systematic errors. An increase in helium abundance has similar effects on the model predictions as an increase in surface gravity, i.e. a pressure rise through the increase in mean molecular weight (Kudritzki 1973). A list of spectral lines (helium and metals) analysed in the present

Table 2. Stellar parameters of Deneb.

Name	Deneb
Spectral type	A2 Ia
d	802 ± 66 pc
Radial velocity	2.50 km s ⁻¹
Atmosphere	
T_{eff}	8525 ± 75 K
$\log g$ (cgs)	1.10 ± 0.05
$n(\text{He})$ (number fraction)	0.11 ± 0.01
$[M/H]$	-0.20 ± 0.04
ξ	8 ± 1 km s ⁻¹
ζ	20 ± 2 km s ⁻¹
$v \sin i$	20 ± 2 km s ⁻¹
Photometry	
V^a	$1^m 25$
$B - V^a$	$+0^m 09$
$U - B^a$	$-0^m 23$
$(B - V)_0^b$	$0^m 05$
$E(B - V)$	$0^m 04$
A_V	$0^m 11$
$(m_V - M_V)_0^c$	$9^m 52 \pm 0^m 18$
M_V	$-8^m 38 \pm 0^m 18$
$B.C.^b$	$-0^m 11$
M_{bol}	$-8^m 49 \pm 0^m 18$
Physical	
$\log L / L_{\odot}$	5.30 ± 0.07
R / R_{\odot}	203 ± 17
$M^{\text{spec}} / M_{\odot}$	19 ± 4
$M^{\text{ZAMS}} / M_{\odot}$	23 ± 2
$M^{\text{evol}} / M_{\odot}$	18 ± 2
Wind parameters	
\dot{M}	$3.1 \cdot 10^{-7} M_{\odot} \text{ yr}^{-1}$
v_{∞}^d	240 ± 25 km s ⁻¹
β	3.0
$\xi_{\text{H}\alpha}$	35 km s ⁻¹

^a Johnson et al. (1966); ^b calculated from the ATLAS9 model;

^c Humphreys (1978); ^d Hirsch (1998)

study can be found in the Appendix³. The photospheric hydrogen Balmer lines from H_{β} to H_8 are analysed, and in addition numerous Paschen, Brackett, and Pfund lines. H_{α} is omitted in the derivation of the basic atmospheric parameters as it is strongly affected by wind emission.

We derive the atmospheric parameters in an iterative process from our set of hydrogen, helium, magnesium, and nitrogen lines. The results (and further information on Deneb) are summarised in Table 2. The agreement between theory and observation for these final parameters and the response of some of the diagnostic lines to variations at the amount of the derived uncertainties (75 K in T_{eff} and 0.05 in $\log g$) are illustrated in Figs. 2 and 3.

The microturbulent velocity is determined primarily from the N I lines on the condition that the abundance indicated by a line does not depend on its equivalent width. This condition is also fulfilled for all elements with non-LTE calculations, as discussed later (Fig. 6). Macroturbulence and $v \sin i$ are derived by detailed line-profile fits to features of various elements.

³ Appendix A is only available in electronic form at <http://www.edpsciences.org>

² <http://ines.laef.esa.es/>

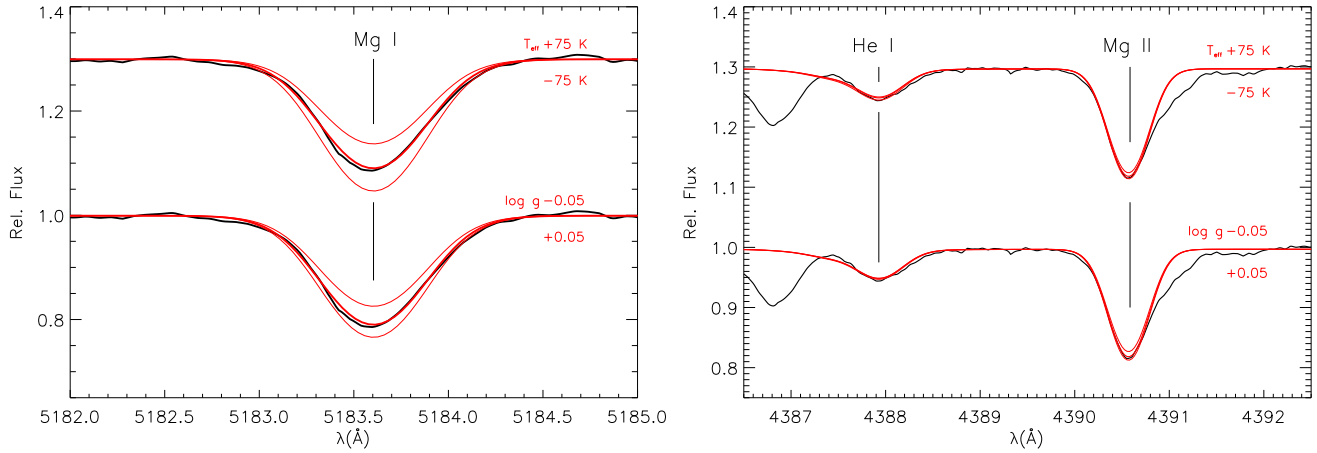


Fig. 2. Temperature determination for Deneb using the Mg I/II non-LTE ionisation equilibrium. Displayed are the observed line profiles for some strategic lines, Mg I λ 5183 (*left panel*) and Mg II λ 4390 and He I λ 4387 (*right panel*), and the best fit for stellar parameters as given in Table 2 (thick red line); theoretical profiles for varied parameters are also shown (thin red lines, as indicated). A vertical shift by 0.3 units has been applied to the upper set of profiles. Note the strong sensitivity of the minor ionic species, Mg I, to parameter changes, while Mg II is virtually unaffected.

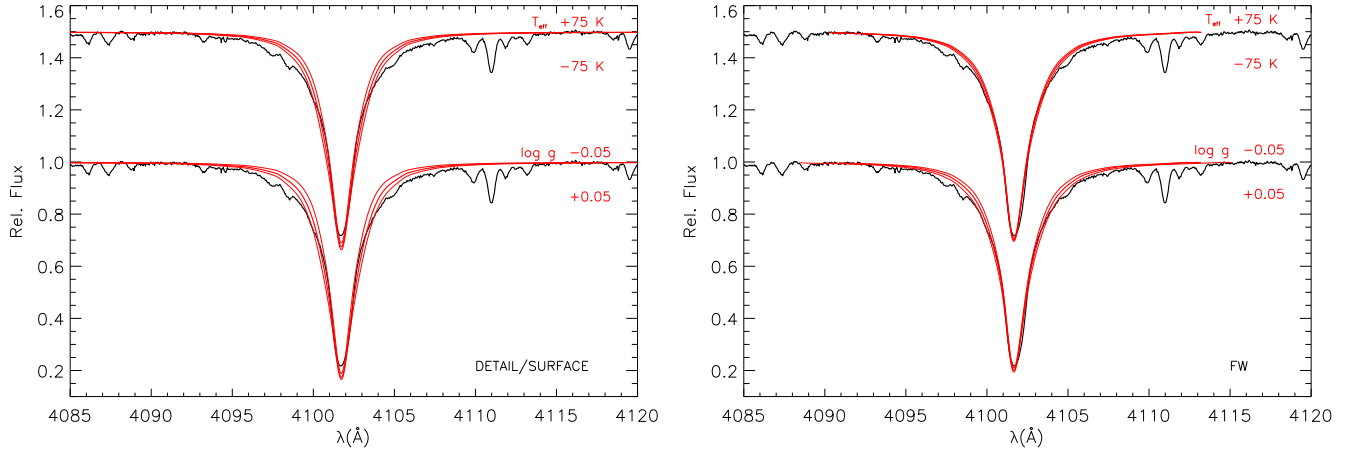


Fig. 3. Impact of stellar parameter variations on non-LTE line profile fits (*left panel*). Synthetic spectra for the adopted parameters (see Table 2, thick red line) and varied parameters as indicated (thin red lines) are compared to observations. A vertical shift by 0.5 units has been applied to the upper profiles. *Right panel*: observation and spectrum synthesis with FASTWIND for $\log g = 1.12$ dex (central line) and two variations as indicated. Note that, although the hydrodynamical FASTWIND model produces a better agreement with the observation, the resulting parameters of both methods are practically identical.

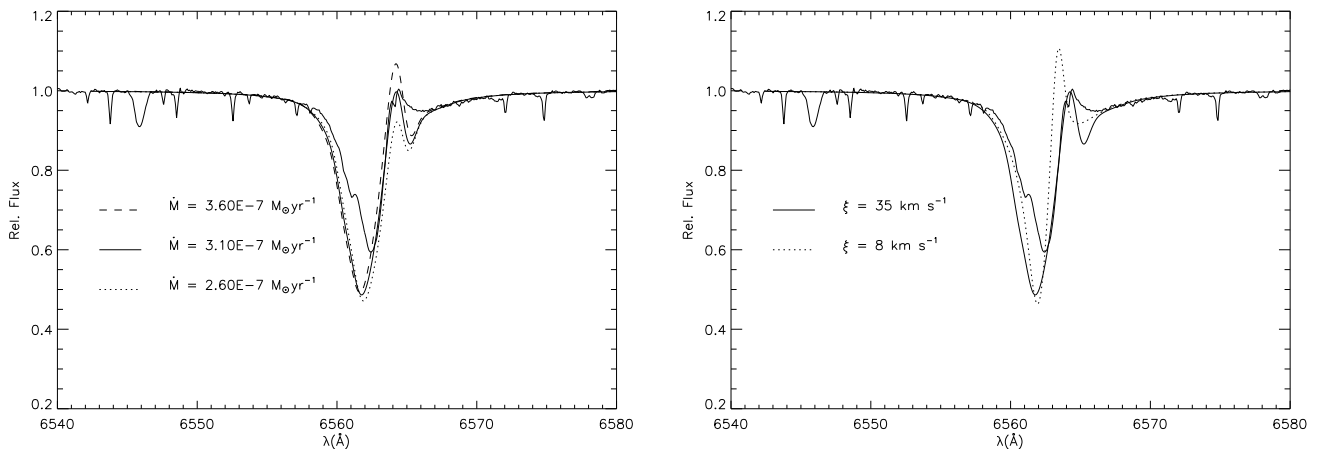


Fig. 4. Impact of variations in mass-loss rate and turbulent velocity on H α model spectra (computed with FASTWIND). The final model was calculated with the wind parameters in Table 2.

Table 3. Stellar parameters of Deneb from different sources.

Source	T_{eff} in K	$\log g$	ξ in km s^{-1}
<i>This work</i>	8525 ± 75	1.10 ± 0.05	8 ± 1
Blackwell et al. (1980)	7635	–	–
Bonneau et al. (1981)	8250 8150 ± 600	–	–
Aufdenberg et al. (2002)	8600 ± 500 8420 ± 100	1.3 1.1–1.6	15 –
Albayrak (2000)	9000	1.45	3.6–11.9
Takeda et al. (1996)	9000	1.5	10
Samedov (1993)	9100	1.2	–
Groth (1961)	9170 ± 500	1.13 ± 0.2	–
Zverko (1971)	9510	1	11 / 17
Aydin (1972)	9900	1.2 ± 0.2	5–12
Takeda (1994)	10000	1.5	10
Burnashev (1980)	10080	1.54	–

Only a fair compromise could be achieved when fitting the cores and the wings of the Balmer lines simultaneously with our hybrid non-LTE technique. Figure 3 (left panel) shows an example. This prompted us to perform test calculations with FASTWIND (Puls et al. (2005) in order to obtain hydrodynamic, line-blanketed non-LTE models in spherical geometry. Specification of stellar mass-loss rate \dot{M} , wind end velocity v_{∞} , exponent of the velocity law β , and stellar radius R is required as input parameters. Improved matches between models and observation are achieved, see Figs. 3 and 11. The wind parameters can be constrained from $H\alpha$ -profile fitting, see e.g. McCarthy et al. (1997) for details and Fig. 4 for examples in the present case. The wind end velocity is a mean value from the analysis of UV resonance lines in 17 IUE spectra (Hirsch 1998). Recent developments in stellar wind physics like in particular wind clumping (so far not investigated in A-type supergiants) and possible effects of a weak magnetic field (Verdugo et al. 2002, 2005) are not considered, such that the derived wind parameters may be subject to revision in the future. The need for a higher turbulent velocity than in the photospheric analysis, in order to reproduce the emission peak and remaining discrepancies in matching the absorption trough of $H\alpha$, are indicators that additional effects may need to be considered in the modelling. However, this is beyond the scope of the present paper. Note also that, at present, FASTWIND does not consider line formation for the metal ions relevant for A-type stars.

So far, several analyses of Deneb’s atmosphere have been performed. The derived values of atmospheric parameters show a remarkable spread, as summarised in Table 3. Values for the effective temperature range from 7635 to 10080 K, with most studies indicating T_{eff} around 9000 to 10000 K. Our determination indicates a low T_{eff} , which is in excellent agreement with the comprehensive study of Aufdenberg et al. (2002). The $\log g$ also shows a remarkable spread with our result being lower than in most of the other studies. Finally, our value for the microturbulent velocity falls roughly in the middle of the range discussed in the literature. In contrast to several previous analyses, we derive a unique value for ξ from all ions. Also, no depth dependency of microturbulence is found in the photospheric analysis.

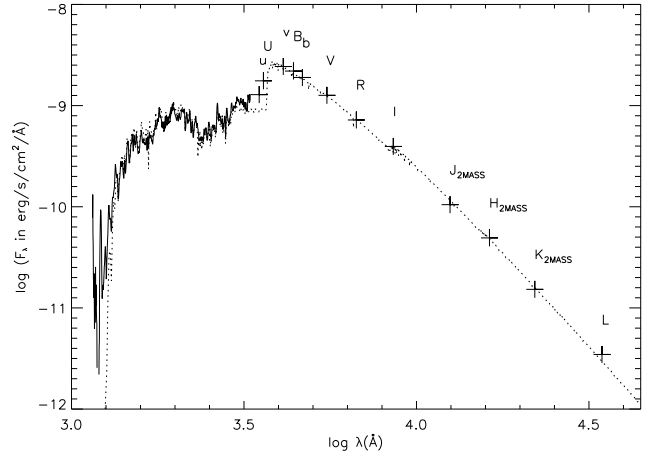


Fig. 5. Comparison of the ATLAS9 model flux (dotted line) with UV-spectra from IUE (full line) and with measurements in various magnitude systems (Johnson, Strömgren, 2MASS). The theoretical flux is calculated for our final parameters (Table 2). The SEDs are normalised in V .

3.2. Spectral energy distribution

We verify our results from the spectral line analysis of Deneb by comparing our model flux (from ATLAS9) with the observed spectral energy distribution (SED). Several sources of observational data are considered (see Sect. 2). We transform $m_1, b-y, c_1$ to Strömgren magnitudes u, v, b, y assuming $V = y$. The various magnitudes are transformed into fluxes by adopting zero points according to Heber et al. (2002, their Table 3). The observed fluxes are dereddened using a reddening law as described by Cardelli et al. (1989), assuming a ratio of extinction to colour excess $A_V/E(B-V) = 3.1$. An overall good to excellent agreement between observed and computed SED is achieved, see Fig. 5.

3.3. Fundamental stellar parameters

Finally, the spectral analysis allows us to determine the fundamental stellar parameters of Deneb, i.e. its luminosity L , mass M , and radius R . Adopting a distance modulus of $9^m52 \pm 0^m18$ from the affiliation of Deneb to the Cyg OB 7 association (mean value of Humphreys 1978), we derive the absolute visual magnitude and, using a bolometric correction from our model atmosphere computations, the absolute bolometric magnitude. The resulting values for L , R , and M are summarised in Table 2. Excellent consistency is achieved with R derived from the mean uniform-disk angular diameter measurement of Deneb by Aufdenberg et al. (2002) assuming the same distance.

We can obtain an independent distance estimate by applying of the flux-weighted gravity-luminosity relationship (FGLR, Kudritzki et al. 2003). The FGLR allows the absolute bolometric magnitude of BA-type supergiants to be derived from a measurement of T_{eff} and $\log g$. We infer a distance modulus $(m_V - M_V)_0$ of $9^m41 \pm 0^m23$ with the FGLR, in good agreement with Humphreys (1978).

4. Abundances

4.1. Results of the present analysis

We determine the abundances of several astrophysically interesting elements in non-LTE (He, C, N, O, Mg, S, Ti, and Fe) and abundances of the remaining detectable species in LTE. The

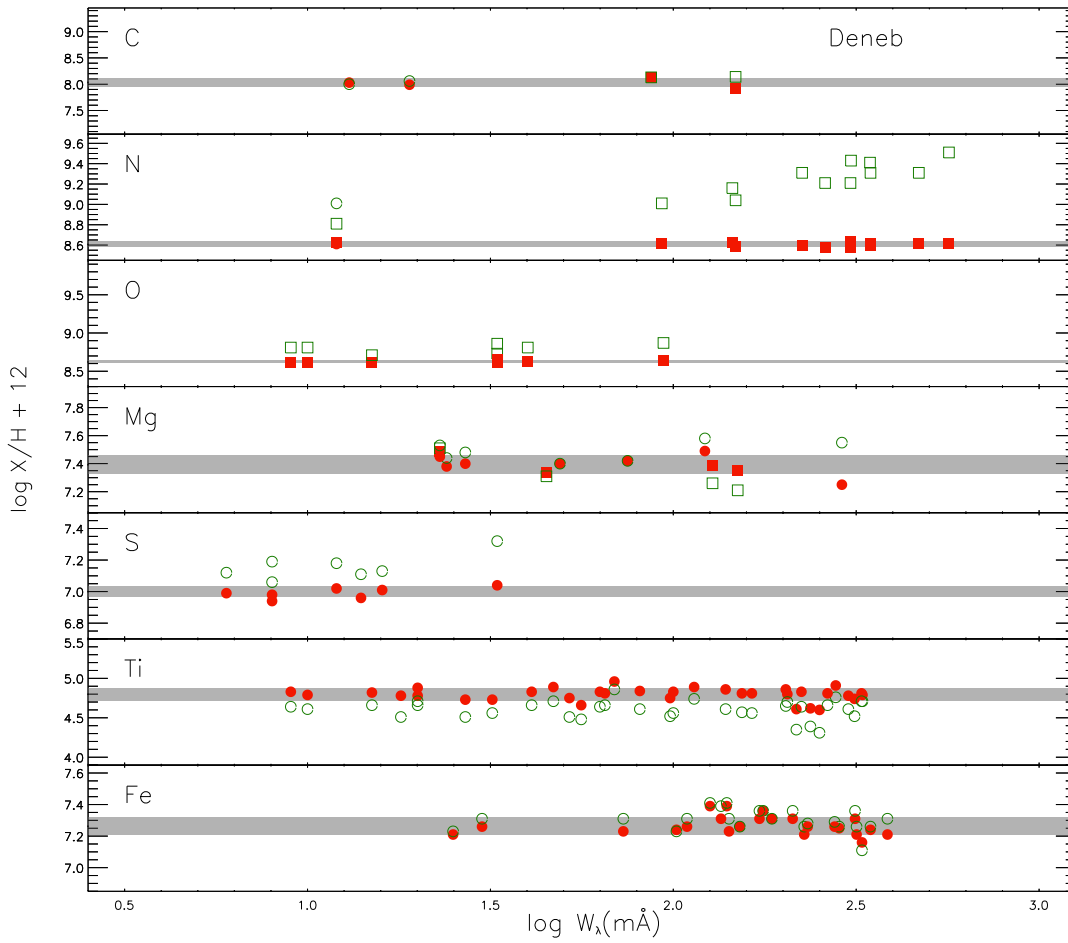


Fig. 6. An overview of non-LTE and LTE abundances for individual lines of all metals treated in non-LTE. The abundance derived from a single line is presented versus its equivalent width, if measurable. Filled red symbols indicate non-LTE abundances, empty green ones LTE abundances. Moreover, squares mean neutral species, circles single-ionized species. For each element, the non-LTE mean value with statistical uncertainties of all lines (including those analysed only by spectrum synthesis) is represented by grey bands.

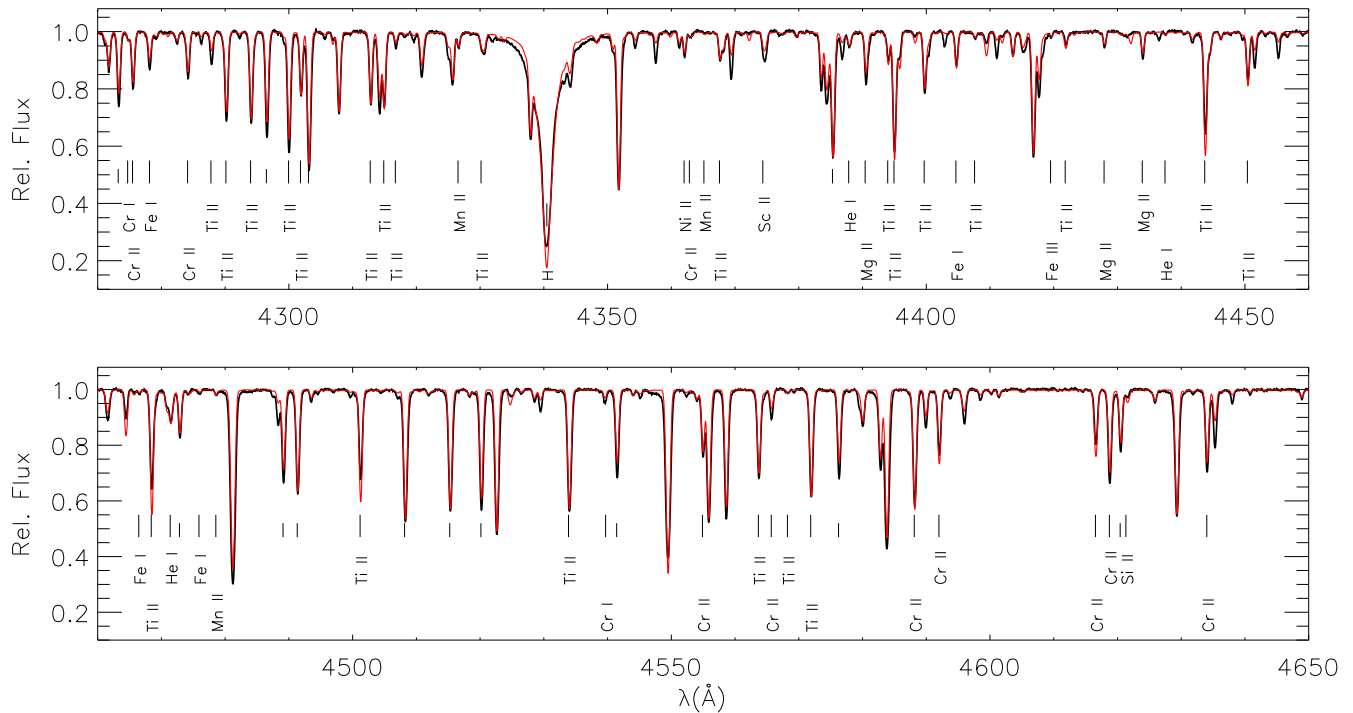


Fig. 7. Comparison of our spectrum synthesis (thin red line) with the high-resolution spectrum of Deneb (full black line). The spectral features used for our abundance determination are identified, short vertical marks designate Fe II lines.

analysis is based on detailed line-profile fits; equivalent widths are only measured as supplementary information. Details of the

results from the analysis of individual lines can be found in the Appendix. In the following, all abundance values are given in

Table 4. Mean non-LTE and LTE abundances/statistical uncertainties.

Ion	$\log \epsilon_{\text{non-LTE}}$	$\log \epsilon_{\text{LTE}}$	# lines
He I	11.09 ± 0.02	–	8
C I	8.02 ± 0.11	8.09 ± 0.08	3
C II	8.05 ± 0.07	8.06 ± 0.07	3
N I	8.61 ± 0.03	9.19 ± 0.24	13
N II	8.61	9.01	1
O I	8.62 ± 0.02	8.80 ± 0.07	15
Ne I	–	8.17 ± 0.02	4
Na I	–	7.02 ± 0.11	3
Mg I	7.39 ± 0.07	7.32 ± 0.13	4
Mg II	7.39 ± 0.07	7.49 ± 0.07	8
Al I	–	5.98 ± 0.06	2
Al II	–	6.11 ± 0.18	2
Si II	–	7.67 ± 0.09	7
S II	7.00 ± 0.03	7.18 ± 0.09	10
Ca II	–	5.79 ± 0.20	3
Sc II	–	2.38 ± 0.11	2
Ti II	4.80 ± 0.08	4.60 ± 0.11	40
V II	–	3.58 ± 0.03	8
Cr I	–	5.68 ± 0.08	5
Cr II	–	5.63 ± 0.08	39
Mn I	–	5.40	1
Mn II	–	5.39 ± 0.04	11
Fe I	–	7.20 ± 0.05	20
Fe II	7.26 ± 0.06	7.29 ± 0.07	28
Fe III	–	7.28	1
Ni II	–	6.19 ± 0.05	7
Sr II	–	2.03 ± 0.04	2
Ba II	–	2.03	1

the usual logarithmic notation $\log \epsilon(\text{el}) = \log (x_{\text{el}}/x_{\text{H}}) + 12$, i.e. as number fractions x_{el} relative to hydrogen.

A comparison of the non-LTE and LTE abundances (i.e. considering and neglecting non-LTE effects), where possible, is shown in Fig. 6. The differences between non-LTE and LTE can be rather small in some cases, like carbon (usually below ~ 0.05 dex). However, in other cases like N and S, they can be larger (on the mean ~ 0.6 and ~ 0.2 dex, respectively), demonstrating the improvements by the non-LTE computations. Proper non-LTE calculations reduce the line-to-line scatter to only a few percent and remove systematic trends present in the LTE results. The S and Ti abundances show systematic differences in non-LTE and LTE. LTE abundances can be systematically higher like in the case of S, whereas the situation for Ti is reversed. Mean non-LTE and LTE abundances of iron are in rather good agreement. The LTE analysis indicates larger statistical uncertainties in practically all cases. It is usually assumed that non-LTE effects occur only in strong lines. Note, however, that even weak lines can show considerable departures from LTE as can be seen e.g. in the case of nitrogen. Overall, similar trends for non-LTE effects, as in other Galactic BA-type supergiants (Przybilla et al. 2006), are found.

Mean non-LTE and LTE abundances are summarised in Table 4. The statistical uncertainties of the non-LTE results are typically (much) smaller than for the LTE values. These small statistical uncertainties and the simultaneous establishment of all ionisation equilibria in non-LTE, i.e. a high degree of self-consistency, are characteristic for our analysis. As a consequence, excellent agreement between our final synthetic spectrum and observations is found (except for a few features), see Fig. 7 for an example.

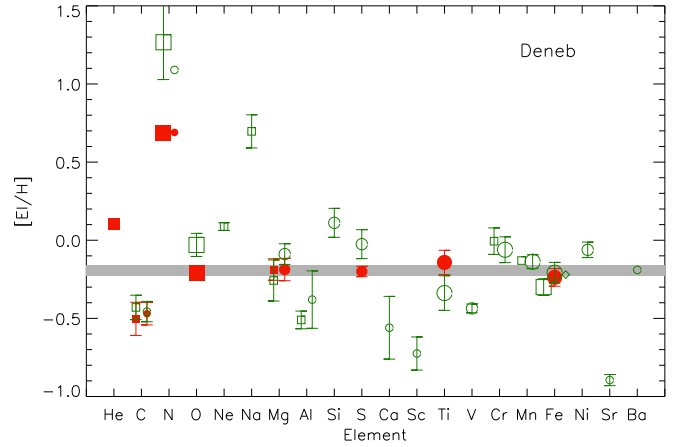


Fig. 8. Results from the elemental abundance analysis (relative to the solar composition, Grevesse & Sauval 1998) for Deneb. Filled symbols denote non-LTE, open symbols LTE results. Boxes: neutral; circles: single-ionized; diamonds: double-ionized species. The symbol size codes the number of spectral lines analysed - small: 1 to 5; medium: 6 to 10; large: more than 10. Error bars represent 1σ -uncertainties from the line-to-line scatter. The grey-shaded area marks the deduced metallicity of Deneb within 1σ -errors. The non-LTE abundance analysis reveals abundances of -0.20 ± 0.04 dex (relative to solar composition) for all heavier elements in close agreement.

The results of our abundance analysis relative to the solar standard (Grevesse & Sauval 1998, meteoritic abundances favoured) are shown in Fig. 8. Combined with a slight overabundance of He (0.10 dex), the strong overabundance of N (0.69 dex), and the C-deficiency of 0.49 dex indicate pronounced mixing with CN-processed matter from the stellar core. We obtain an N/C ratio of 4.44 ± 0.84 and an N/O ratio of 0.86 ± 0.06 (each by mass fraction). The implications of this abundance pattern on the evolutionary status of Deneb will be discussed in Sect. 6. Non-LTE abundances of oxygen and heavier elements show consistently sub-solar values of -0.20 ± 0.04 dex. A significant scatter around this mean value is found for the remaining elements, where only LTE abundances are available. The abundance pattern is analogous to the one in other Galactic BA-type supergiants (Przybilla et al. 2006), but at significantly reduced metallicity. Future non-LTE investigations of those elements have to decide whether some of these deviations are intrinsic or whether they indicate systematic errors made by assuming of LTE for the line-formation calculations.

4.2. Comparison with previous analyses

Quantitative analyses of the chemical composition of Deneb are rare in the literature. The pioneering study of Groth (1961) derives an abundance pattern similar to ours, but it systematically finds larger abundances. Compared to our choice of the solar values, he finds an He-excess of 0.64 dex, a C-depletion by -0.33 dex, and an N-/O-excess of 1.48 and 0.53 dex, respectively, as well as overabundances for other metals of typically ~ 0.3 – 0.4 dex. While outstanding for that time, the results of Groth have to be critically reviewed in the context of improved model atmospheres and atomic data.

The most recent abundance analysis of Deneb is provided by Albayrak (2000). His results are summarised in Fig. 9. The pure LTE analysis finds striking features like an He-deficiency

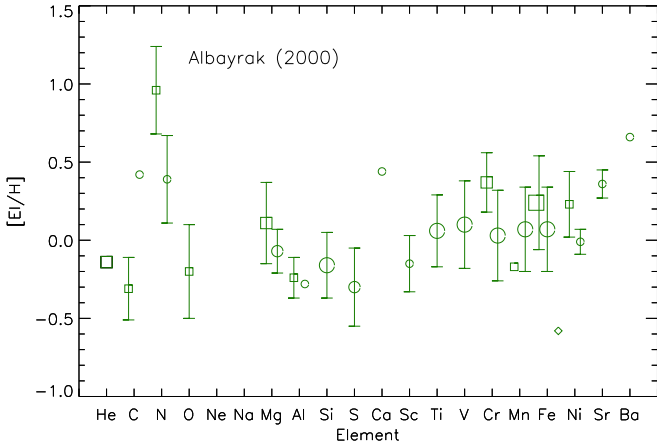


Fig. 9. Same as Fig. 8, for the LTE analysis of Albayrak (2000). Larger statistical uncertainties become apparent than in our non-LTE, and even our LTE analysis and systematic effects occur. Striking features are the He-*deficiency* and discrepancies in some ionisation equilibria (e.g. C I/II and Fe I/II vs. Fe III).

and large differences in abundances from different ions of an element, i.e. a failure to establish some of the ionisation equilibria. Albayrak’s analysis indicates a roughly solar composition on the mean, with the abundances of the heavier elements tending to be slightly supersolar. However, the abundance determination gives large statistical uncertainties and shows a wide spread around the solar standard, which in view of our findings can be interpreted as systematic uncertainties. These may be the consequence of a combination of systematically biased stellar parameters – in particular the higher T_{eff} (see Table 3) will result in larger abundances for most of the ionic species – and the neglect of non-LTE effects.

Takeda et al. (1996) also provide an analysis of elemental abundances in Deneb, partially in non-LTE (Fig. 10). They derive a moderate N-excess by 0.3 dex and a significant C-deficiency of about 0.5 dex relative to the solar standard, in moderate agreement with our results. Helium tends to be *depleted* by 0.14 dex; however, an uncertainty of 0.43 dex renders any conclusion difficult. The heavy elements (Na and S) show super-solar abundances, while oxygen is significantly sub-solar. The higher T_{eff} adopted in the work of Takeda et al. (see Table 3) will result in systematically larger abundances like in the case of Albayrak (2000).

The direct comparison of Fig. 8 with Figs. 9 and 10 demonstrates the drastic (note the logarithmic scale) reduction of statistical *and* systematic uncertainties in the present work. The existence of abundance patterns like those derived in the two other abundance studies are difficult to explain in terms of a) massive star evolution: mixing with CN-cycled matter results in helium enhancement; and b) galactochemical evolution: massive stars in the solar neighbourhood have slightly sub-solar, not (markedly) super-solar, metallicities (see e.g. Table 4 of Przybilla et al. 2006). The present work leads to more conservative conclusions, as we find a uniform pattern consistent with a metallicity of -0.2 dex.

5. Near-IR spectroscopy

Aufdenberg et al. (2002) provide an analysis of the (near-)IR spectrum of Deneb reporting some discrepancies in particular concerning the Pfund series of hydrogen that was fitted for the

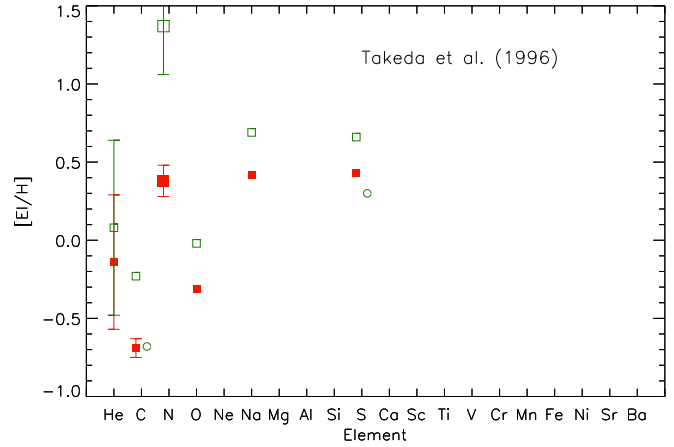


Fig. 10. Same as Fig. 8, for the results of Takeda et al. (1996). Non-LTE calculations were made only for neutral species. Note that He tends to be depleted, while the heavier elements indicate super-solar abundances, unlike our results.

first time. Thus, we also test our modelling in the same spectral regions, which are scarcely considered in quantitative analyses of A-type supergiants. The high-quality near-IR spectra of Fullerton & Najarro (1998) (a comprehensive data set like this one is unavailable for any other A-type supergiant) are a key element in our analysis.

Consistency in the analysis of visual and near-IR spectra is not easily achieved because of the amplification of non-LTE effects in the Rayleigh-Jeans tail of the spectral energy distribution. This results in a high sensitivity of the spectral lines not only to details in the atmospheric structure but also to the details of the model atoms used in the statistical equilibrium calculations. For hydrogen, this requires reliable cross-sections for excitation by electron impact in particular (Przybilla & Butler 2004), in addition to the accurately known atomic data for radiative transitions.

Good to excellent agreement between spectrum synthesis with DETAIL/SURFACE (photospheric lines) and FASTWIND (wind-affected lines) and the observations is achieved comprising multiple features of the Paschen, Brackett, and Pfund series in addition to the traditionally utilised Balmer lines, as summarised in Fig. 11. Neither LTE nor non-LTE modelling based on collisional data derived from classical approximation formulae succeeds in obtaining this self-consistency (see also Przybilla & Butler 2004 for a detailed discussion). This resolves the discrepancies reported by Aufdenberg et al. (2002).

6. Evolutionary status

Massive stars are important drivers of the chemodynamic evolution of galaxies and their interstellar medium. A detailed investigation of these topics requires quantitative understanding of the evolution of massive stars in general and of the advanced stages in their lives in particular. In the following we want to discuss our results for the benchmark A-type supergiant Deneb in the context of the stellar evolution models available at present.

A Hertzsprung-Russell diagram (HRD) is shown in Fig. 12. Evolution tracks for rotating and non-rotating stars according to Meynet & Maeder (2003) are displayed. Starting with an initial N/C ratio (by mass) of 0.31, the stars may experience rotationally-induced mixing of the atmospheric layers with nuclear-processed material. Predicted N/C ratios at the end of

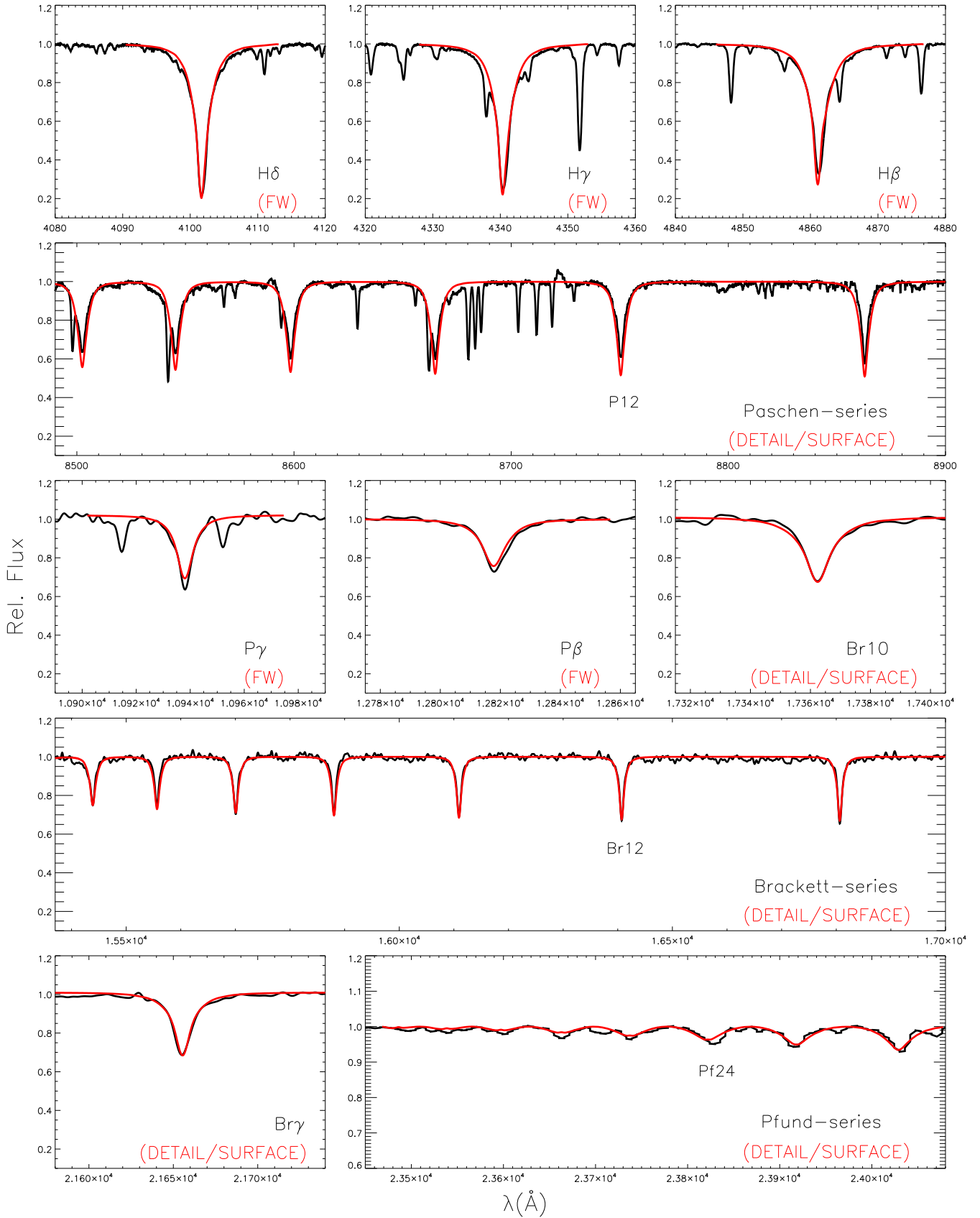


Fig. 11. Modelling (red) of the hydrogen lines in the visual and the near-IR (black curve). The synthetic spectra are calculated with our hybrid non-LTE technique using DETAIL/SURFACE (photospheric lines) or FASTWIND (FW, wind-affected lines), as indicated. Except for the Pfund series, all panels show the same range in relative flux. Some lines, such as P β and H β , are noticeably affected by the stellar wind.

H-burning, in the blue supergiant stage (at $T_{\text{eff}} = 10\,000\text{ K}$), and in the red supergiant stage after the first dredge-up are also displayed. Deneb falls between the tracks for zero-age main-sequence (ZAMS) masses of 20 and $25\ M_{\odot}$ and shows a much more pronounced N/C ratio than predicted. The value is also much higher than in similar supergiants analysed with the same method (Przybilla et al. 2006). This leaves us with two possible scenarios for Deneb's state of evolution.

In the first scenario, Deneb started its life as a late O-type star with $M^{\text{ZAMS}} = 23 \pm 2\ M_{\odot}$ on the main sequence and is currently evolving to the red supergiant stage. The second scenario implies a more advanced stage of an $M^{\text{ZAMS}} \approx 20 \pm 2\ M_{\odot}$ star after the red supergiant phase, which may also lead it through the blue supergiant regime (Hirschi et al. 2004). In this case Deneb's atmosphere should expose abundance ratios for the light elements typical of the first dredge-up phase.

The two scenarios may be distinguished by a comparison of spectroscopic and evolutionary masses and by the light element abundances. The first scenario implies an evolutionary mass of $M^{\text{evol}} \approx 18 \pm 2\ M_{\odot}$, in excellent agreement with the derived $M^{\text{spec}} \approx 19 \pm 4\ M_{\odot}$, whereas the predicted mass in the second scenario, $M^{\text{evol}} \approx 11\ M_{\odot}$, is inconsistent with M^{spec} . At first glance, the observed high N/C ratio agrees better with a first dredge-up scenario, though helium would be underabundant. However, the predicted surface abundances depend on the assumed initial rotational velocity of the star. The tracks follow the evolution of a massive star with typical initial angular momentum, i.e. with a fixed rotational velocity of 300 km s^{-1} . If the star rotates even faster, the He abundance and the N/C ratio may be higher. This may even be enhanced further by the interplay of rotation with a magnetic field (Maeder & Meynet 2005).

We conclude that Deneb is a star evolving from the main sequence to the red supergiant stage. Because of its pronounced mixing signature with nuclear-processed matter, its main-sequence progenitor was probably an initially fast rotator.

7. Summary and conclusions

A detailed and comprehensive model atmosphere analysis of the prototype A-type supergiant Deneb was performed. We derived basic atmospheric parameters, elemental abundances, and fundamental stellar parameters as summarised in Tables 2 and 4 using a hybrid non-LTE spectrum synthesis technique, as well as line-blanketed hydrodynamic non-LTE models. High consistency in the results was achieved, bringing all indicators simultaneously into match: multiple metal ionisation equilibria, Stark-broadened hydrogen lines from the Balmer to Pfund series, and the spectral energy distribution from the UV to the near-IR. The results were obtained with high internal accuracy.

Our detailed non-LTE abundance analysis reveals an abundance pattern typical of the mixing of the atmosphere with CN-processed matter from the stellar core, i.e. He- and N-enrichment combined with C-depletion. Non-LTE abundances of the heavier elements consistently show a value of ~ 0.20 dex below the solar standard, exhibiting none of the peculiar patterns reported in earlier analyses.

The evolutionary status of Deneb was constrained from a comparison of the observed properties with stellar evolution models. The spectroscopic mass, the surface He abundance, and a high N/C ratio are indicative of the evolution of an initially fast-rotating main-sequence star towards the red supergiant stage.

Acknowledgements. We would like to thank U. Heber for his support and interest in the project, as well as for many useful comments on the manuscript.

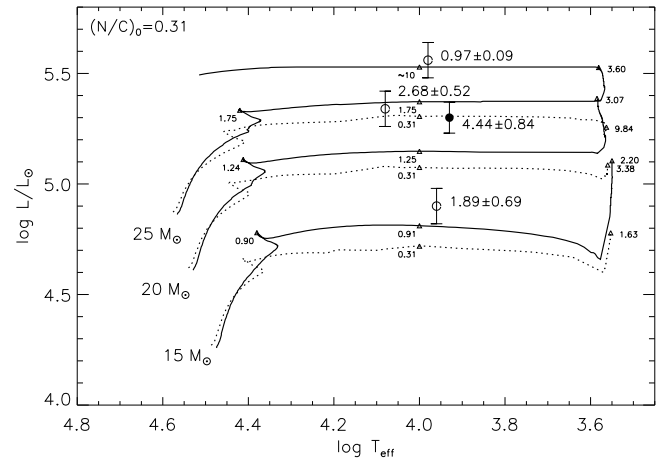


Fig. 12. Stellar evolution tracks (Meynet & Maeder 2003) in the HRD for different ZAMS masses of stars with an initial rotational velocity of 300 km s^{-1} (full lines) and 0 km s^{-1} (dotted lines) and solar metallicity until the end of central helium burning. Observed N/C ratios (large numbers) are displayed for a few objects: Deneb (dot) and three stars from Przybilla et al. (2006, open circles). Small numbers along the curves indicate the progression of N/C-ratios (mass fractions) in the course of evolution, assuming an initial value of 0.31 (solar). The N/C ratios at the red supergiant stage mark the situation at the end of central helium burning, with the exception of the $25\ M_{\odot}$ model with rotation which enters the Wolf-Rayet phase near the end of central helium burning.

We thank A.W. Fullerton for providing the high-quality infrared spectra in the Jw-, H-, and K-band. We also thank A.F. Gulliver for making available an electronic version of a spectral atlas of Deneb. We are grateful to K. Butler for making DETAIL and SURFACE available and to J. Puls for making FASTWIND available. F. Schiller would like to acknowledge the financial support of the "Studienstiftung des deutschen Volkes" which makes this project feasible throughout the Ph.D. phase.

References

- Albayrak, B. 2000, *A&A*, 364, 237
- Albayrak, B., Gulliver, A.F., Adelman, S.J., Aydin, C., & Kocer, D. 2003, *A&A*, 400, 1043
- Aufdenberg, J.P., Hauschildt, P.H., Baron, E. et al. 2002, *ApJ*, 570, 344
- Aydin, C. 1972, *A&A* 19, 369
- Barnard, A.J., Cooper, L., & Shamey, L.J. 1969, *A&A*, 1, 28
- Bates, D., & Damgaard, A. 1949, *Phil. Trans. R. Soc. London, Ser. A*, 242, 101
- Becker, S.R. 1998, in *Boulder-Munich II, Properties of Hot, Luminous Stars*, ed. I.D. Howarth (San Francisco: ASP), 137
- Blackwell, D.E., Petford A.D., & Shallis M.J. 1980, *A&A*, 82, 249
- Bonneau, D., Koehler, L., Oneto, J. L., & Vakili, F. 1981, *A&A*, 103, 28
- Bresolin, F., Kudritzki, R.-P., Méndez, R.H., & Przybilla, N. 2001, *ApJ*, 548, L159
- Bresolin, F., Gieren, W., Kudritzki, R.P., Pietrzyński, G., & Przybilla, N. 2002, *ApJ*, 567, 277
- Burnashev, V.I. 1980, *Izv. Krym. Astrofiz. Obs.* 3, 62
- Butler, K., & Giddings, J.R. 1985, in *Newsletter on Analysis of Astronomical Spectra*, No. 9 (London, Univ. London)
- Butler, K., Mendoza, C., & Zeippen, C.J. 1993, *J. Phys. B*, 26, 4409
- Cardelli, J.A., Clayton, G.C., & Mathis, J.S. 1989, *ApJ*, 345, 245
- Cowley, C. 1971, *Observatory*, 91, 139
- Davidson, M.D., Snoek, L.C., Volten, H., & Dönszelmann, A. 1992, *A&A*, 255, 457
- Dimitrijević, M.S., & Sahal-Bréchet, S. 1990, *A&AS*, 82, 519
- Dimitrijević, M.S., & Sahal-Bréchet, S. 1996, *A&AS*, 117, 127
- Dimitrijević, M.S., & Sahal-Bréchet, S. 1997, *A&AS*, 122, 163
- Fuhr, J.R., & Wiese, W.L. 1998, in *CRC Handbook of Chemistry and Physics*, 79th ed., ed. D.R. Lide (Boca Raton: CRC Press)

- Fuhr, J.R., Martin, G.A., & Wiese, W.L. 1988, *J. Phys. & Chem. Ref. Data*, Vol. 17, Suppl. 4
- Fullerton, A.W., & Najarro, F. 1998, in *Boulder-Munich II, Properties of Hot, Luminous Stars*, ed. I.D. Howarth (San Francisco: ASP), 47
- Giddings, J.R. 1981, Ph. D. thesis, Univ. London
- Grevesse, N., & Sauval, A.J. 1998, *Space Sci. Rev.*, 85, 161
- Griem, H.R. 1964, *Plasma Spectroscopy* (New York: McGraw-Hill Book Company)
- Griem, H.R. 1974, *Spectral Line Broadening by Plasmas* (New York and London: Academic Press)
- Groth, H.-G. 1961, *ZAp*, 51, 231
- Hauck, B., & Mermilliod, M. 1998, *A&AS*, 129, 431
- Heber, U., Moehler, S., Napiwotzki, R., Thejll, R., & Green, E.M. 2002, *A&A*, 383, 938
- Heger, A., & Langer, N. 2000, *ApJ*, 544, 1016
- Heger, A., Woosley, S. E., & Spruit, H. C. 2005, *ApJ*, 626, 350
- Hirsch, S. 1998, Diploma Thesis, Univ. Munich
- Hirschi, R., Meynet, G., & Maeder, A. 2004, *A&A*, 425, 649
- Humphreys, R.M. 1978, *ApJS*, 38, 309
- Johnson, H. L., Mitchell, R. I., Iriarte, B., & Wisniewskj, W. Z. 1966, *Comm. Lunar Plan. Lab.*, 4, 99
- Kaufert, A., Stahl, O., Wolf, B., et al. 1996, *A&A*, 305, 887
- Kudritzki, R.P. 1973, *A&A*, 28, 103
- Kudritzki, R.P., Puls, J., Lennon, D.J., et al. 1999, *A&A*, 350, 970
- Kudritzki, R.P., Bresolin, F., & Przybilla, N. 2003, *ApJ*, 582, L83
- Kurucz, R.L. 1993, Kurucz CD-ROM No. 13 (Cambridge, Mass.: Smithsonian Astrophysical Observatory)
- Kurucz, R.L., & Bell, B. 1995, Kurucz CD-ROM No. 23 (Cambridge, Mass.: Smithsonian Astrophysical Observatory)
- Lanz, T., Dimitrijević, M.S., & Artru, M.-C. 1988, *A&A*, 192, 249
- Maeder, A., Meynet, G. 2005, *A&A*, 440, 1041
- Martin, G.A., Fuhr, J.R., & Wiese, W.L. 1988, *J. Phys. & Chem. Ref. Data*, Vol. 17, Suppl. 3
- McCarthy, J.K., Kudritzki, R.P., Lennon, D.J., Venn, K.A., & Puls, J. 1997, *ApJ*, 482, 757
- Meynet, G., & Maeder, A. 2003, *A&A*, 404, 975
- Morel, M., & Magnenat, P. 1978, *A&AS*, 34, 477
- Nieva, M.F., & Przybilla, N. 2006, *ApJ*, 639, L39
- Nieva, M.F., & Przybilla, N. 2008, *A&A*, accepted, arXiv:0711.3783 [astro-ph]
- Pfeiffer, M. J., Frank, C., Baumüller, D., Fuhrmann, K., & Gehren, T. 1998, *A&AS*, 130, 381
- Przybilla, N. 2002, Ph. D. Thesis, Univ. Munich
- Przybilla, N. 2005, *A&A*, 443, 293
- Przybilla, N., & Butler, K. 2001, *A&A*, 379, 955
- Przybilla, N., & Butler, K. 2004, *ApJ*, 609, 1181
- Przybilla, N., Butler, K., Becker, S.R., Kudritzki, R.P., & Venn, K.A. 2000, *A&A*, 359, 1085
- Przybilla, N., Butler, K., Becker, S.R., & Kudritzki, R.P. 2001a, *A&A*, 369, 1009
- Przybilla, N., Butler, K., & Kudritzki, R. P. 2001b, *A&A*, 379, 936
- Przybilla, N., Butler, K., Becker, S.R., & Kudritzki R.P. 2006, *A&A*, 445, 1099
- Puls, J., Urbaneja, M.A., Venero, R. et al. 2005, *A&A* 435, 669
- Samedov, Z.A. 1993, *AZh*, 70, 82
- Sigut, T.A.A. 1999, *ApJ*, 519, 303
- Skrutskie, M. F., Cutri, R. M., Stiening, R., et al. 2006, *AJ*, 131, 1163
- Stehlé, C., & Hutcheon, R. 1999, *A&AS*, 140, 93
- Takeda, Y. 1994, *PASJ*, 46, 181
- Takeda, Y., Takada-Hidai, M., & Kotake, J. 1996, *PASJ*, 48, 753
- Urbaneja, M.A., Herrero A., Bresolin F., et al. 2005, *ApJ*, 622, 862
- Verdugo, E., Gómez de Castro, A., Ferro-Fontán, C., & Talavera, A. 2002, in *Radial and Nonradial Pulsations as Probes of Stellar Physics*, ed. C. Aerts, T. R. Bedding, & J. Christensen-Dalsgaard (San Francisco: ASP), 574
- Verdugo, E., Henrichs, H. F., Talavera, A., et al. 2005, in *The Nature and Evolution of Disks Around Hot Stars*, ed. R. Ignace & K. G. Gayley (San Francisco: ASP), 324
- Vidal, C.R., Cooper, J., & Smith, E.W. 1973, *ApJS*, 25, 37
- Vrancken, M., Butler, K., & Becker, S.R. 1996, *A&A*, 311, 661
- Wallace, L., & Hinkle, K. 1997, *ApJS*, 111, 445
- Wiese, W.L., Smith, M.W., & Glennon, B.M. 1966, *Nat. Stand. Ref. Data Ser., Nat. Bur. Stand. (U.S.), NSRDS-NBS 4, Vol. I*
- Wiese, W.L., Smith, M.W., & Miles, B.M. 1969, *Nat. Stand. Ref. Data Ser., Nat. Bur. Stand. (U.S.), NSRDS-NBS 22, Vol. II*
- Wiese, W.L., Fuhr, J.R., & Deters, T.M. 1996, *J. Phys. & Chem. Ref. Data, Mon. 7*
- Zverko, J. 1971, *Bull. astr. Inst. Czechosl.*, 22, 49

Online Material

Appendix A: Spectral line analysis

In this appendix we provide details on our spectral line analysis, as a basis for further interpretation. Table A1 summarises our line data and the results from the abundance analysis for Deneb. The first columns give the transition wavelength λ (in Å), excitation energy of the lower level χ (in eV), adopted oscillator strength $\log gf$, an accuracy indicator, and the source of the gf value. Then, for each line the measured equivalent width W_λ (in mÅ) is tabulated, followed by the derived abundance $\log \varepsilon = \log(X/H)+12$. In cases with an entry for the non-LTE abundance correction $\Delta \log \varepsilon = \log \varepsilon_{\text{non-LTE}} - \log \varepsilon_{\text{LTE}}$ this denotes the non-LTE abundance, otherwise the LTE abundance. The equivalent widths have been measured by direct integration over the spectral lines. In some cases metal lines are situated in the wings of the Balmer lines. Then their equivalent width is measured with respect to the *local* continuum, indicated by 'S(W_λ)'. Abundances are determined from a best match of the spectrum synthesis to the observed line *profiles* and not the equivalent widths. Spectrum synthesis also allows blended features to be used for abundances determinations, where a W_λ measurement is hampered. These cases are marked by a single 'S' in Table A1. For He I, only non-LTE abundances are derived because of the potential of this major atmospheric constituent to change atmospheric structure and thus the stellar parameter determination.

Table A1 Spectral line analysis

$\lambda(\text{\AA})$	χ (eV)	$\log gf$	Acc.	Src.	$W_\lambda(\text{m\AA})$	$\log \varepsilon$	$\Delta \log \varepsilon$
He I:							
4026.18	20.96	-2.63	A	WSG	22	11.09	...
4026.19	20.96	-0.63	A	WSG			
4026.20	20.96	-0.85	A	WSG			
4026.36	20.96	-1.32	A	WSG			
4120.81	20.96	-1.74	B	WSG	34	11.12	...
4120.82	20.96	-1.96	B	WSG			
4120.99	20.96	-2.44	B	WSG			
4387.93	21.22	-0.88	A	WSG	S	11.13	...
4437.55	21.22	-2.03	B	WSG	5	11.09	...
4471.47	20.96	-0.20	A	WSG	S	11.07	...
4471.49	20.96	-0.42	A	WSG			
4471.68	20.96	-0.90	A	WSG			
4713.14	20.96	-1.23	B	WSG	30	11.10	...
4713.16	20.96	-1.45	B	WSG			
4713.38	20.96	-1.93	B	WSG			
5015.68	20.62	-0.82	AA	WSG	S	11.09	...
5875.60	20.96	-1.52	A	WSG	101	11.06	...
5875.61	20.96	0.48	A	WSG			
5875.63	20.96	-0.34	A	WSG			
5875.64	20.96	0.14	A	WSG			
5875.97	20.96	-0.22	A	WSG			
C I:							
4771.74	7.49	-1.87	C	WFD	87	8.13	0.00
5052.17	7.68	-1.45	B	WFD	S	8.00	0.00
9088.51	7.48	-0.43	B	WFD	148	7.92	-0.22
C II:							
4267.00	18.05	0.56	C+	WFD	19	7.99	-0.07
4267.26	18.05	0.74	C+	WFD			
6578.05	14.45	-0.03	B	WFD	S(13)	8.03	0.03
6582.88	14.45	-0.33	B	WFD	S	8.13	0.00
N I:							
6008.47	11.60	-1.11	C+	WFD	12	8.63	-0.18
7423.64	10.33	-0.71	B+	WFD	145	8.63	-0.53
7442.30	10.33	-0.38	B+	WFD	225	8.60	-0.71
7468.31	10.34	-0.19	B+	WFD	306	8.64	-0.79
7898.98	12.36	0.02	C	WFD	S	8.55	-0.16
7899.28	12.36	-0.91	C	WFD			
8567.74	10.68	-0.66	B	WFD	S(148)	8.59	-0.45
8680.28	10.34	0.35	B+	WFD	S(567)	8.62	-0.89
8683.40	10.33	0.09	B+	WFD	S(469)	8.62	-0.69
8686.15	10.33	-0.31	B+	WFD	S(347)	8.62	-0.79
8703.25	10.33	-0.32	B+	WFD	305	8.58	-0.63
8711.70	10.33	-0.23	B+	WFD	346	8.60	-0.71
8718.84	10.34	-0.34	B+	WFD	260	8.58	-0.63
8728.90	10.33	-1.07	B+	WFD	S(93)	8.62	-0.39
N II:							
3995.00	18.50	0.21	B	WFD	12	8.61	-0.40
O I:							
3947.29	9.15	-2.10	B	WFD	33	8.61	-0.12
3947.48	9.15	-2.24	B	WFD			
3947.59	9.15	-2.47	B	WFD			
4654.12	10.74	-2.16	C+	WFD	S	8.61	-0.10
4654.56	10.74	-1.93	C+	WFD			
4772.45	10.74	-1.92	C+	WFD	S	8.61	-0.10
4772.91	10.74	-1.70	C+	WFD			
4773.75	10.74	-1.55	C+	WFD	S	8.61	-0.10

Table A1 (cont.)

λ (Å)	χ (eV)	log gf	Acc.	Src.	W_λ (mÅ)	log ε	$\Delta \log \varepsilon$
O I:							
4967.38	10.74	-1.63	C+	WFD	15	8.61	-0.10
4967.88	10.74	-1.41	C+	WFD			
5329.10	10.74	-1.24	C+	WFD	40	8.63	-0.18
5329.68	10.74	-1.02	C+	WFD			
5330.73	10.74	-0.87	C+	WFD	33	8.66	-0.20
5435.18	10.74	-1.78	C+	WFD	10	8.61	-0.20
5435.77	10.74	-1.54	C+	WFD			
5436.86	10.74	-1.39	C+	WFD	9	8.61	-0.20
6046.23	10.99	-1.76	C+	WFD	S	8.61	-0.20
6046.44	10.99	-1.54	C+	WFD			
6046.49	10.99	-2.24	C+	WFD			
6155.96	10.74	-1.36	B+	WFD	S	8.63	-0.18
6155.97	10.74	-1.01	B+	WFD			
6155.99	10.74	-1.12	B+	WFD			
6156.74	10.74	-1.49	B+	WFD			
6156.76	10.74	-0.90	B+	WFD			
6156.78	10.74	-0.69	B+	WFD			
6158.15	10.74	-1.84	B+	WFD	94	8.64	-0.23
6158.17	10.74	-1.00	B+	WFD			
6158.19	10.74	-0.41	B+	WFD			
6453.60	10.74	-1.29	C+	WFD	S	8.61	-0.35
6454.44	10.74	-1.07	C+	WFD			
7001.90	10.99	-1.49	B	WFD	S	8.61	-0.25
7001.92	10.99	-1.01	B	WFD			
7002.17	10.99	-2.66	B	WFD			
7002.20	10.99	-1.49	B	WFD			
7002.23	10.99	-0.74	B	WFD			
7002.25	10.99	-1.36	B	WFD			
7254.15	10.99	-1.27	C+	WFD	S	8.66	-0.17
7254.45	10.99	-1.05	C+	WFD			
7254.53	10.99	-1.74	C+	WFD			
Ne I:							
5852.49	16.85	-0.49	B	S	5	8.14	...
6143.06	16.62	-0.10	B	S	7	8.16	...
6266.50	16.72	-0.37	B	S	5	8.17	...
6402.20	16.62	0.33	B	S	15	8.20	...
Na I:							
4982.81	2.10	-0.91	D	WSM	S	7.13	...
5682.63	2.10	-0.70	C	WSM	S	7.00	...
8194.79	2.10	-0.44	D	WSM	60	6.92	...
8194.82	2.10	0.51	C	WSM			
Mg I:							
4702.99	4.35	-0.42	C+	BMZ	23	7.49	-0.02
5172.68	2.71	-0.38	B	WSM	128	7.39	+0.13
5183.60	2.72	-0.16	B	WSM	150	7.35	+0.14
8806.76	4.35	-0.16	C+	BMZ	45	7.34	+0.03
Mg II:							
4390.51	10.00	-1.71	D	WSM	122	7.49	-0.09
4390.57	10.00	-0.53	D	WSM			
4427.99	10.00	-1.20	C+	WSM	27	7.40	-0.08
4433.99	10.00	-0.90	C+	WSM	49	7.40	0.00
4739.71	11.57	-0.66	C+	T	24	7.38	-0.06
4739.71	11.57	-0.77	C+	T			
4851.08	11.63	-0.42	C	CA	S(23)	7.45	-0.08
6545.97	11.63	0.41	C	CA	S(75)	7.42	0.00
7877.05	10.00	0.39	C+	WSM	S	7.35	-0.18
7896.04	10.00	-0.30	C+	WSM	289	7.25	-0.30
7896.37	10.00	0.65	C+	WSM			

Table A1 (cont.)

λ (Å)	χ (eV)	log gf	Acc.	Src.	W_λ (mÅ)	log ε	$\Delta \log \varepsilon$
Al I:							
3944.01	0.00	-0.64	C+	WSM	64	6.02	...
3961.52	0.01	-0.34	C+	WSM	80	5.94	...
Al II:							
4663.05	10.60	-0.29	C	WSM	S	6.24	...
5593.30	13.26	0.41	D	WSM	S	5.98	...
Si I:							
4128.07	9.84	0.31	C	WSM	S	7.73	...
4130.89	9.84	0.49	C	WSM	264	7.71	...
4621.42	12.53	-0.54	D	WSM	18	7.47	...
4621.70	12.53	-1.68	D	WSM			
4621.72	12.53	-0.39	D	WSM			
5041.02	10.07	0.17	X	MEL	201	7.70	...
5688.81	14.16	0.16	X	MEL	S	7.72	...
5957.56	10.07	-0.35	D	WSM	S	7.65	...
5978.93	10.07	-0.06	D	WSM	143	7.72	...
Si II:							
4142.26	15.85	0.24	D-	WSM	S	7.04	-0.16
4153.07	15.90	0.62	D-	WSM	12	7.02	-0.16
4162.67	15.94	0.78	D-	WSM	14	6.96	-0.15
4716.27	13.62	-0.41	D	WSM	8	6.94	-0.12
4815.55	13.67	0.09	D	WSM	16	7.01	-0.12
4917.20	14.00	-0.32	D	WSM	6	6.99	-0.13
5320.72	15.07	0.50	D	WSM	8	6.98	-0.21
5428.66	13.58	-0.13	D	WSM	S	7.00	-0.10
5453.86	13.67	0.48	D	WSM	33	7.04	-0.28
5660.00	13.68	-0.05	D	WSM	S	7.02	-0.32
Ca I:							
4799.97	8.44	-0.42	C	SA	S	6.02	...
8248.80	7.51	0.57	C-	WSM	50	5.65	...
8912.07	7.05	0.57	X	KB	103	5.70	...
Sc II:							
4246.82	0.32	0.28	D	KB	143	2.30	...
4374.46	-0.44	-0.64	D	KB	S	2.45	...
Ti II:							
3900.56	1.13	-0.45	D	MFW	329	4.79	+0.08
3913.48	1.12	-0.53	D	MFW	301	4.78	+0.17
3987.60	0.61	-2.73	D	MFW	20	4.78	+0.12
4025.13	1.13	-0.45	D	MFW	S	4.76	+0.25
4028.36	1.89	-1.00	D	MFW	114	4.89	+0.15
4287.88	1.08	-2.02	D-	MFW	69	4.96	+0.10
4290.22	1.16	-1.12	D-	MFW	203	4.86	+0.21
4290.35	2.06	-1.53	X	KB			
4294.09	1.08	-1.11	D-	MFW	205	4.80	+0.10
4300.06	1.18	-0.77	D-	MFW	278	4.91	+0.15
4301.92	1.16	-1.16	D-	MFW	164	4.81	+0.25
4312.87	1.18	-1.16	D-	MFW	154	4.81	+0.24
4314.97	1.16	-1.13	D-	MFW	S	4.81	+0.24
4316.80	2.05	-1.42	D	MFW	65	4.81	+0.15
4330.24	2.04	-1.51	D	MFW	S(63)	4.83	+0.19
4330.72	1.18	-2.04	D-	MFW			
4367.66	2.59	-0.72	X	KB	S	4.81	+0.25
4394.02	1.22	-1.59	D-	MFW	52	4.75	+0.24
4395.00	1.08	-0.66	D-	MFW	313	4.74	+0.22
4399.79	1.24	-1.27	D-	MFW	139	4.86	+0.25
4407.68	1.22	-2.47	D-	MFW	15	4.82	+0.16

Table A1 (cont.)

$\lambda(\text{\AA})$	χ (eV)	$\log gf$	Acc.	Src.	$W_\lambda(\text{m\AA})$	$\log \varepsilon$	$\Delta \log \varepsilon$
Ti II:							
4421.90	2.05	-1.39	X	KB	27	4.73	+0.22
4443.78	1.08	-0.70	D-	MFW	237	4.62	+0.23
4450.50	1.08	-1.45	D-	MFW	98	4.75	+0.23
4468.52	1.13	-0.60	D-	MFW	251	4.60	+0.29
4501.27	1.11	-0.75	D-	MFW	217	4.61	+0.26
4533.97	1.24	-0.77	D-	MFW	327	4.81	+0.10
4563.77	1.22	-0.96	D-	MFW	224	4.83	+0.19
4568.31	1.22	-2.65	D	MFW	9	4.83	+0.19
4571.96	1.57	-0.53	D-	MFW	264	4.81	+0.15
4708.67	1.24	-2.21	D	MFW	18	4.78	+0.27
4763.81	1.22	-2.45	X	KB	S	4.86	+0.15
4798.53	1.08	-2.43	X	KB	S	4.78	+0.27
4874.01	3.09	-0.79	D	MFW	41	4.83	+0.17
4911.19	3.12	-0.34	D	MFW	56	4.66	+0.18
5069.09	3.12	-1.39	D	MFW	10	4.79	+0.18
5072.28	3.12	-0.75	D	MFW	32	4.73	+0.17
5129.15	1.89	-1.39	D	MFW	47	4.89	+0.18
5185.91	1.89	-1.61	D	MFW	81	4.84	+0.23
5188.68	1.58	-1.21	D	MFW	100	4.83	+0.27
5336.77	1.58	-1.70	D	MFW	S	4.88	+0.22
5381.02	1.57	-2.08	D	MFW	20	4.88	+0.17
V II:							
3916.42	1.43	-1.06	B	MFW	S	3.60	...
3951.97	1.48	-0.74	B	MFW	67	3.53	...
4005.71	1.82	-0.46	D	MFW	S	3.59	...
4023.39	1.80	-0.52	X	KB	60	3.57	...
4035.63	1.79	-0.62	X	KB	53	3.58	...
4036.78	1.47	-1.54	D	MFW	15	3.61	...
4065.07	3.78	-0.24	X	KB	10	3.62	...
4183.44	2.05	-0.95	X	KB	S	3.57	...
Cr I:							
4274.80	0.00	-0.23	B	MFW	S	5.67	...
4539.76	2.54	-1.15	B	MFW	25	5.81	...
5204.51	0.94	-0.20	B	MFW	S	5.65	...
5206.04	0.94	0.02	B	MFW	S	5.58	...
5208.41	0.94	0.16	B	MFW	12	5.71	...
Cr II:							
3979.51	5.65	-0.73	X	KB	S(73)	5.59	...
4037.97	6.49	-0.56	X	KB	41	5.60	...
4054.08	3.11	-2.47	X	KB	S	5.64	...
4072.56	3.70	-2.41	X	KB	28	5.60	...
4086.13	3.71	-2.42	X	KB	24	5.51	...
4132.11	11.47	-2.19	X	KB	S	5.65	...
4132.42	3.74	-2.35	X	KB			
4145.78	5.30	-1.16	X	KB	77	5.77	...
4207.34	3.81	-2.48	X	KB	19	5.48	...
4242.36	3.87	-1.33	X	KB	192	5.71	...
4252.63	3.84	-2.02	X	KB	S	5.72	...
4261.91	3.87	-1.53	X	KB	148	5.66	...
4269.28	3.85	-2.17	X	KB	52	5.67	...
4275.57	3.86	-1.71	X	KB	104	5.71	...
4284.19	3.86	-1.86	X	KB	95	5.72	...
4362.92	5.64	-1.89	X	KB	S	5.77	...
4555.01	4.07	-1.38	D	MFW	S	5.68	...
4565.74	4.04	-2.11	D	MFW	53	5.79	...
4588.22	4.07	-0.63	D	MFW	286	5.62	...

Table A1 (cont.)

$\lambda(\text{\AA})$	χ (eV)	$\log gf$	Acc.	Src.	$W_\lambda(\text{m\AA})$	$\log \varepsilon$	$\Delta \log \varepsilon$
Cr II:							
4592.07	4.07	-1.22	D	MFW	141	5.52	...
4616.64	4.07	-1.29	D	MFW	S	5.50	...
4618.82	4.07	-1.11	D	MFW	222	5.75	...
4634.10	4.07	-1.24	D	MFW	184	5.76	...
4812.34	3.86	-1.99	X	KB	61	5.61	...
4824.12	3.87	-0.96	X	KB	244	5.62	...
4836.22	3.86	-1.99	X	KB	68	5.62	...
4836.94	3.09	-1.13	B	MFW			
4848.24	3.86	-1.14	X	KB	S(224)	5.59	...
4876.41	3.86	-1.46	D	MFW	178	5.61	...
4884.58	3.86	-2.08	D	MFW	53	5.60	...
4901.62	6.49	-0.83	X	KB	25	5.57	...
5237.33	4.06	-1.16	D	MFW	195	5.54	...
5246.76	3.71	-2.45	D	MFW	23	5.61	...
5310.69	4.07	-2.28	D	MFW	25	5.63	...
5313.61	4.07	-1.65	D	MFW	101	5.62	...
5334.87	4.05	-1.56	X	KB	81	5.48	...
5420.91	3.76	-2.36	D	MFW	26	5.50	...
5478.37	4.16	-1.91	X	KB	63	5.68	...
5508.63	4.16	-2.11	D	MFW	39	5.62	...
5620.63	6.46	-1.14	X	KB	12	5.62	...
6053.47	4.74	-2.16	D	MFW	16	5.60	...
Mn I:							
4034.48	0.00	-0.81	C+	MFW	S	5.40	...
Mn II:							
4206.37	5.40	-1.57	X	KB	17	5.34	...
4326.16	5.40	-1.25	X	KB	30	5.42	...
4365.22	6.57	-1.35	X	KB	S	5.39	...
4478.64	6.65	-0.95	X	KB	12	5.42	...
4755.73	5.40	-1.24	X	KB	29	5.40	...
4784.63	6.57	-1.51	X	KB	5	5.41	...
4806.82	5.42	-1.56	X	KB	10	5.28	...
5297.00	9.86	-0.21	X	KB	7	5.40	...
5297.03	9.86	0.43	X	KB			
5297.06	9.86	0.62	X	KB			
5302.40	9.87	0.23	X	KB	S	5.43	...
5302.43	9.87	1.00	X	KB			
5559.05	6.19	-1.32	X	KB	S	5.41	...
5570.54	6.18	-1.44	X	KB	S	5.42	...
Fe I:							
3872.50	0.99	-0.92	B+	FMW	139	7.11	...
3872.92	2.72	-1.75	C	FMW			
3895.66	0.11	-1.67	B+	FMW	S	7.16	...
3899.71	0.09	-1.53	B+	FMW	S	7.21	...
3918.42	2.79	-1.01	X	KB	57	7.16	...
3922.91	0.05	-1.65	B+	FMW	30	7.16	...
3927.92	0.11	-1.59	C	FMW	37	7.23	...
3930.30	0.09	-1.59	C	FMW	S	7.23	...
4045.81	1.48	0.28	B+	FMW	132	7.16	...
4063.59	1.56	0.07	C+	FMW	94	7.13	...
4071.74	1.61	-0.65	B+	FMW	70	7.15	...
4147.34	3.32	-1.90	X	KB	11	7.21	...
4147.49	3.32	-2.47	B+	FMW			
4147.67	1.48	-2.10	B+	FMW			
4154.50	2.79	-0.48	X	KB	S	7.21	...
4154.81	3.33	-0.37	C+	FMW			

Table A1 (cont.)

λ (Å)	χ (eV)	log gf	Acc.	Src.	W_λ (mÅ)	log ε	$\Delta \log \varepsilon$
Fe I:							
4181.75	2.83	-0.18	D-	FMW	15	7.16	...
4219.36	3.57	0.12	C+	FMW	8	7.21	...
4278.23	3.37	-1.74	C	FMW	75	7.31	...
4404.75	1.56	-0.14	B+	FMW	63	7.19	...
4466.55	2.83	-0.59	C+	FMW	S	7.31	...
4476.02	2.79	-0.73	X	KB	S	7.26	...
4476.08	3.59	-0.37	X	KB			
4871.32	2.87	-0.41	C+	FMW	S(39)	7.21	...
4918.95	4.10	-0.67	X	KB	11	7.23	...
4918.99	2.87	-0.37	C+	FMW			
Fe II:							
3938.29	1.67	-3.89	D	FMW	S	7.23	-0.03
4031.44	4.73	-3.12	X	KB	S	7.21	+0.02
4051.21	5.52	-2.99	X	KB	S	7.26	± 0.00
4122.64	2.58	-3.38	D	FMW	176	7.36	± 0.00
4173.46	2.58	-2.18	C	FMW	328	7.16	+0.05
4273.32	2.70	-3.34	D	FMW	152	7.26	± 0.00
4296.57	2.70	-3.01	D	FMW	228	7.21	-0.05
4303.17	2.70	-2.49	C	FMW	284	7.25	-0.01
4385.39	2.78	-2.57	D	FMW	S	7.25	± 0.00
4472.62	7.65	-2.34	X	KB	102	7.24	+0.01
4489.19	2.83	-2.23	D	FMW	186	7.31	± 0.00
4491.40	2.86	-2.70	C	FMW	233	7.26	-0.02
4508.28	2.86	-2.31	D	KB	346	7.24	-0.02
4515.34	2.84	-2.48	D	FMW	276	7.26	-0.03
4520.23	2.81	-2.60	D	FMW	314	7.31	-0.05
4541.52	2.86	-3.05	D	FMW	172	7.31	-0.05
4576.33	2.84	-3.04	D	FMW	212	7.31	-0.05
4620.51	2.83	-3.28	D	FMW	142	7.23	-0.08
4656.97	2.89	-3.63	E	FMW	73	7.23	-0.08
4993.35	2.81	-3.65	E	FMW	S	7.21	-0.05
5074.05	6.75	-1.97	X	KB	30	7.26	-0.05
5197.48	5.89	-2.72	X	KB	317	7.21	-0.05
5197.58	3.23	-2.79	C	FMW			
5254.93	3.14	-3.23	X	KB	109	7.26	-0.05
5276.00	3.20	-1.94	C	FMW	385	7.21	-0.10
5427.83	6.72	-1.66	X	KB	25	7.21	-0.02
6147.74	3.89	-2.72	X	KB	140	7.39	-0.02
6149.26	3.89	-2.72	X	KB	126	7.39	-0.02
6238.39	3.89	-2.63	X	KB	135	7.31	-0.08
Fe III:							
4419.60	8.24	-2.22	X	KB	10	7.28	...
Ni II:							
4015.47	4.03	-2.42	X	KB	76	6.19	...
4067.03	4.03	-1.84	X	KB	163	6.12	...
4192.07	4.03	-3.06	X	KB	26	6.22	...
4244.78	4.03	-3.11	X	KB	22	6.19	...
4362.10	4.03	-2.72	X	KB	44	6.21	...
4679.16	6.84	-1.75	X	KB	14	6.26	...
5065.98	12.29	0.01	X	KB	10	6.13	...
5066.06	14.33	-0.83	X	KB			
Sr II:							
4077.71	0.00	0.15	X	FW	104	2.00	...
4215.52	0.00	-0.17	X	FW	77	2.05	...
Ba II:							
4554.03	0.00	0.14	X	D	S	2.03	...

accuracy indicators – uncertainties within: AA: 1%; A: 3%; B: 10%; C: 25%; D: 50%; E: larger than 50%; X: unknown

sources of gf -values – BMZ: Butler et al. (1993); CA: Coulomb approximation (Bates & Damgaard 1949); D: Davidson et al. (1992); F: Fernley et al. (available from TOPBASE); FMW: Fuhr et al. (1988); KB: Kurucz & Bell (1995); MEL: Mendoza et al. (available from TOPBASE); MFW: Martin et al. (1988); S: Sigut (1999); T: Taylor (available from TOPBASE); WFD: Wiese et al. (1996); WSG: Wiese et al. (1966); WSM: Wiese et al. (1969); when available^(c), improved gf -values from Fuhr & Wiese (1998) are favoured

sources for Stark broadening parameters – H I: Stehlé & Hutcheon (1999), Vidal et al. (1973); He I: Barnard et al. (1969), Dimitrijević & Sahal-Bréchet (1990); C I: Griem (1974), Cowley (1971); C II: Griem (1964, 1974), Cowley (1971); N I/II: Griem (1964, 1974), Cowley (1971); O I: Cowley (1971); Ne I: Griem (1974), Cowley (1971); Na I: Cowley (1971), Griem (1974); Mg I: Dimitrijević & Sahal-Bréchet (1996), Cowley (1971); Mg II: Griem (1964, 1974), Cowley (1971); Al I: Griem (1974), Cowley (1971); Al II: Griem (1964, 1974), Cowley (1971); Si II: Lanz et al. (1988), Griem (1974), Cowley (1971); S II: Cowley (1971); Ca II: Griem (1974), Cowley (1971); Sc – Ni: Cowley (1971); Sr II: Cowley (1971); Ba II: Dimitrijević & Sahal-Bréchet (1997)